EXPLORING THE MASS DETERMINATION OF ^{33}MG THROUGH THE TIME-OF-FLIGHT TECHNIQUE

by

Pauline McLeod

A thesis submitted in partial fulfilment
of the requirements for the degree of
Bachelor of Science

Saint Mary's University
Halifax, Nova Scotia, Canada

Submitted March 18th, 2013

Abstract

Exploring the mass determination of ^{33}Mg through the time of flight technique
By Pauline McLeod

Neutron-rich unstable isotopes are critical to our understanding of the origins of the heavy elements found on Earth. Their properties, such as mass and binding energy, enable us to look into the nuclear structure, and certain structural anomalies, such as shell closures.

In this experiment, the feasibility of using a time-of-flight technique for mass determination was determined using the neutron-rich isotope ^{33}Mg. ^{33}Mg was chosen due to its close proximity to ^{32}Mg, which experiences a breakdown of the N=20 shell closure.

The mass found for ^{33}Mg did not agree to within uncertainty with the accepted value. The resolution of the mass value was comparable with previous experiments, indicating that through future optimized experiments this technique could prove to be acceptable.

March 18th, 2013

Keywords: Mass determination, time-of-flight, ^{33}Mg, FRS

Contents

List of Figures

Chapter 1

Introduction

Many of the heavy elements found on Earth are believed to have been created in the neutron-rich environments of the universe like neutron stars and supernovae. Short-lived unstable nuclei with large asymmetry of neutrons and protons, deemed rare isotopes, are created through nuclear reactions in these neutron-rich environments, and are thought to be key in understanding the origins of matter around us.

The fundamental properties of these isotopes are yet to be experimentally determined. One of the critical properties of these rare isotopes is a knowledge of its mass. In this work, a case study will be described to explore the possibility of using a time-of-flight technique with high-energy rare isotope beams to determine the mass.

1.1 Nuclear Structure

The physical properties of a nucleus are determined by the configuration of its nucleons. The two types of nucleons, neutral neutrons and positively charged protons, behave according to the electromagnetic and strong interactions.

In order for a nucleus to form, nucleons are densely packed inside the nucleus, allowing them to be bound together by the strong interaction. The strong interaction, while short-ranged, is 100 times greater than the electromagnetic interaction, which allows the positively charged protons to exist in close proximity to each other.

Inside the nucleus, the nucleon density is constant for virtually all nuclei. This is a consequence of the short range of the strong force. Through empirical observations, the mean nuclear radius has been found to increase as a function of nucleon number, A, and can be expressed in femtometres as:

$$R_0 = 1.2 * A^{\frac{1}{3}}.$$

Nucleon-nucleon interactions are complex and cannot be expressed by a simple analytic expression unlike the electromagnetic interaction, but three simple models exist that allow us to learn about the effect of their behaviour on nuclei. The first model is a semi-empirical approach, known as the Liquid Drop Model, that describes the behaviour of the nuclear binding energy as a function of the number of neutrons and protons. The second approach is the Shell Model, which looks at the quantum mechanical behaviour of neutrons and protons. The third approach is known as the Collective Model, which builds upon both the Shell Model and the Liquid Drop Model, but makes the further refinement of including nuclear transitions including many or all of the nucleons in the nucleus [11].

The minimum energy required to completely separate a nucleus into its constituent neutrons and protons is known as the nuclear binding energy [2]. A nucleus with a greater nuclear binding energy tends to be a more stable nucleus. The Liquid Drop Model gives some insight into some of the interactions that take place between

adjacent nucleons, expressed in terms of the binding energy. The model is made up of five terms, and makes the assumption that the nucleus is spherically symmetric and that the nuclear volume is directly related to the number of nucleons present.

The first term, which is dependent on the volume, gives an estimate of the total binding energy that is proportional to the number of nucleons, and results only from the interactions between nucleons and their nearest neighbours; a consequence of the short-range strong force. The second term is the surface term, which shows that nucleons on the surface of the nucleus are less tightly bound due to the fact that they are surrounded by fewer neighbouring nucleons. This term decreases the total energy described by the first term [2].

The third term is the repulsive Coulomb term. Coulomb repulsion occurring between positively charged protons will further decrease the total binding energy of the nucleus. This term would seemingly favour nuclei [2] with large numbers of neutrons as compared to protons, but the fourth term, the symmetry term, states otherwise, that nuclei with equal numbers of protons and neutrons actually tend to be more stable, at least for small A. This can be seen in figure 1.1.

The fifth and final term is the pairing term, which states that nuclei with even numbers of protons and neutrons experience an increase in binding energy, odd-odd nuclei experience a decrease in binding energy, and odd-even even-odd nuclei see no change in binding energy. The sum of these five terms from the Liquid Drop Model gives the total binding energy; this equation is known as the Bethe-Weizsacker mass formula [2]. This is the first and most primitive mass formula available. It follows a macroscopic approach, and while it was used to get insight into the binding energy mechanism of some stable nuclei, it is not accurate enough to explain all detailed features of nuclear masses over the entire nuclear chart. Microscopic approaches, such as

the Skyrme-Hartree Fock mass formulas, account for different pairing strengths with protons and neutrons, among other corrections, but tend not to show shell structures very well. Combined macroscopic-microscopic approaches also exist. The finite-range droplet model is an example of this approach, this model is the go-to standard for mass measurements, and is used as a point of reference for experimentalists. This approach accounts for the different pairing strengths, charge asymmetry, and other corrections while maintaining the shell effects [6].

Nuclei with a strong binding energy are considered stable, as they do not decay. Nuclei that are unstable have weak binding energy, and will only exist for a short period of time that can be expressed by the half-life. They will decay into more stable nuclei through beta decay, where an energetic electron and electron anti-neutrino are emitted, and a neutron is converted to a proton. The energy required to remove a proton or neutron from a nucleus is known as the nucleon separation energy. Stable nuclei have a much higher binding energy than unstable nuclei therefore the nucleon separation energy is correspondingly higher for the stable nucleus.

1.2 Nuclear Shell Model

Similar to electrons occupying shells in atomic structure, evidence has been found supporting the occupation of shells by protons and neutrons inside the nucleus. This behaviour is described by the aptly named shell model. While both electrons and nucleons are fermions, some key differences between the two results in differences in the arrangement and behaviour inside the shells. Firstly, nucleons interact via both the electromagnetic force and the strong force, and, secondly, not all nucleons carry a net charge, only the positive protons.

The evidence for shell structure in the nucleus in part comes from studies of the separation energy as a function of nucleon number. It has been shown that nuclei that contain certain numbers of protons and/or neutrons experience a higher binding energy than predicted by the Liquid Drop Model. These numbers are known as "magic numbers," and correspond to closed shells. Just like an atom with a filled shell of electrons will be more stable against decay than an atom with a partially filled shell, so too will a nucleus with a filled shell be more stable against nuclear decay. Nuclei with magic numbers of both protons and neutrons are exceptionally stable, and are known as "doubly magic" nuclei. Some examples of doubly magic nuclei are the stable isotopes of calcium and oxygen which make life possible on Earth. Magic numbers occur for nuclei with number of neutrons, N, or number of protons, Z, equal to 2, 8, 20, 28, 50, 82, and 126.

Magic numbers arise from gaps in the nuclear energy levels that are due, in large part, to spin-orbit coupling [2]. The potential that nucleons experience in the nucleus can be considered similar to a finite square-well potential. The effects of spin orbit coupling cancels out on the interior of the nucleus, so it is the nucleons at the edges of the nucleus that are of concern. Nucleon energy states can be described by three quantum numbers: n, the principal quantum number, l, the orbital angular momentum quantum number, and j, the total angular momentum quantum number, which is a sum of l and s, the spin quantum number. It is through j that spin-orbit coupling is seen, resulting in a splitting of energy states from l. The degeneracy of these split states is expressed as $2j + 1$. The splitting of the l states causes a reordering of the energy levels, and can be seen in figure 1.2, and results in the gaps that correspond to the magic numbers.

1.3 ^{33}Mg

The shell model holds true for stable nuclei, but as nuclei move further away from stability, the model begins to erode. In some nuclei, such as neutron-rich ^{32}Mg, the conventional arrangement of nuclear orbitals changes. For ^{32}Mg, a breakdown of the N=20 shell closure occurs. The expected binding energy that would be found normally from the shell closure is not available. This is due possibly to a reconfiguration of orbitals [4], known as an "island of inversion". In some cases, the shell closure has been found to have migrated, and the expected shell closure occurs at a non-typical and non-expected nucleon number [5].

By studying the mass of isotopes such as ^{33}Mg around these islands of inversion, insight into the binding energy of nuclei far from stability can be gained.

1.4 Mass Measurement Techniques

There are several methods for directly measuring the mass of nuclei, each with its own advantages and disadvantages. The type of particles being measured, as well as its half-life, plays a large role in whether or not a mass measurement method will be appropriate in the situation.

One method is a linear time of flight technique [7]. It involves a fast in-flight selection of particles based on their mass-to-charge ratio, accomplished through the use of magnetic fields. This technique requires only the magnetic rigidity, derived from position on detectors, and the velocity of an ion in order to determine the mass. It has the advantage of being able to measure very short-lived nuclei, particularly light nuclei. A longer flight path is necessary in order to measure heavy nuclei, and to improve precision with light nuclei. This is the method that was used to obtain

the mass in this experiment, and it will be discussed more in depth in the second chapter.

Another method for determining the mass is through the use of cyclotrons as high-precision mass spectrometers. [7]. This method takes advantage of the fact that the revolution frequency inside a cyclotron is mass dependent, meaning particles with slightly different masses will have slightly different measurable frequencies, allowing particle identification. This method has been employed at GANIL in France for mass measurements far from stability.

A third method that allows the direct measurement of the mass of nuclei is through ion traps. An example of one type of ion trap, a Penning Trap, is TITAN, located at TRIUMF in Vancouver, Canada. Magnetic and electric fields are used to confine ions in a three-dimensional space, then the cyclotron frequency of the particles can be measured to determine the mass. This method is capable of very high-precision measurements, generally on light, stable particles [12].

1.5 Previous experiments in mass determination of ^{33}Mg

Facilities such as GANIL in France perform experiments using the linear time-of-flight technique discussed in the previous section. The motivation of many of these experiments to look at the mass of these exotic nuclei comes from the need to understand the intriguing shell closures and deformations that have been observed.

One experiment, performed in 1991, involved the fragmentation of a ^{48}Ca beam,

and used a direct time-of-flight mass determination technique [8]. In this experiment, the masses of 39 neutron-rich nuclei in the mass range 17 to 37 were measured with the intent to investigate anomalies in the binding energies around the N=20 region. The results from this experiment constituted the first measurements of several of the masses (^{29,30}Ne, ^{34,35}Mg, and ^{36,37}Al) while the majority of the other determinations were the most precise yet made. The majority of the observations were consistent with previous measurements.

The result that is most relevant to this experiment is the determination of the mass excess of ^{33}Mg. From this experiment, the mass excess was found to be 4.85 $\pm$ 0.30 MeV. The uncertainties from this experiment for all nuclei, which ranged from 70 keV to 1600 keV, are stated to be made up of the statistical uncertainty, the uncertainty arising from the calibration, and the uncertainty representing the physical limitations on the precision of the experiment. Other experiments performed at GANIL on light exotic nuclei showed similar mass resolutions [9] [3], with uncertainty values from 100 keV up to 1 MeV. These resolutions can now be used as a guideline for the following experiment for what minimum acceptable resolutions should be obtained.

Figure 1.1: Chart of nuclides, proton number Z vs neutron number N. Figure courtesy of NNDC.

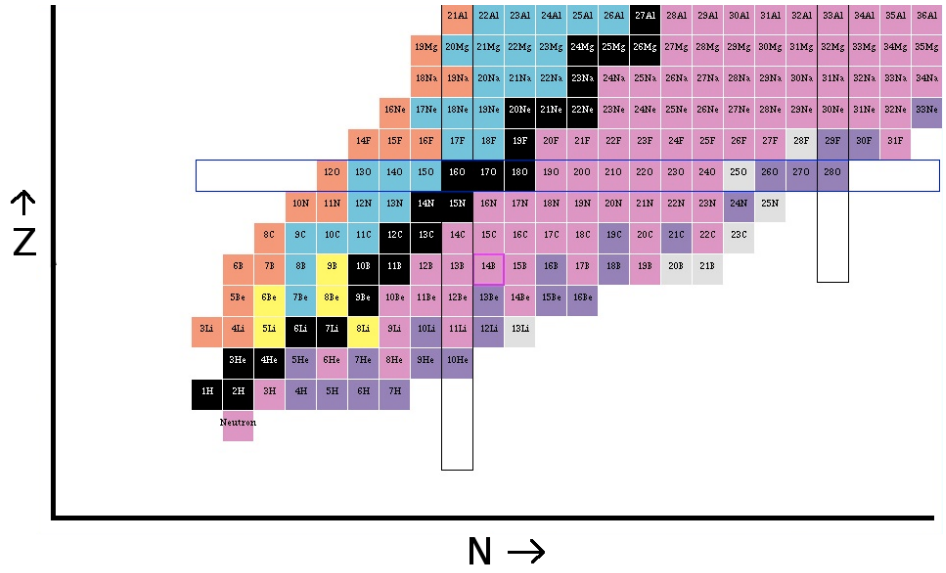

Figure 1.2: Energy levels of a particle in an infinite square well.

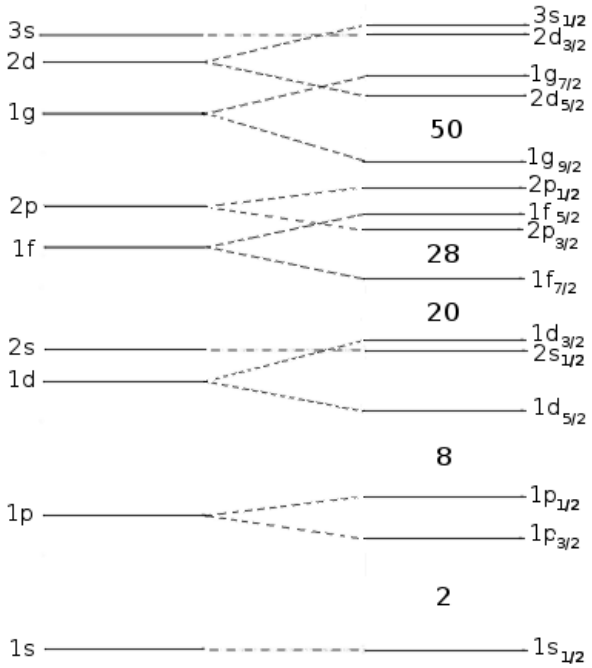

Chapter 2

Experiment

2.1 Theory

The velocity of a particle, v, is dependent on the distance travelled, d, and the time-of-flight (TOF) according to the following equation:

$$v = \frac{d}{TOF}. \tag{2.1}$$

For particles moving with relativistic speed, the velocity can be written in terms of β, the velocity relative to the speed of light. Rearranging and writing in terms of the time of flight, we have

$$\beta = \frac{d}{cTOF}. \tag{2.2}$$

As a charged particle travels through a magnetic field, the direction of its momentum will be deflected. A measure of how difficult a particle is to deflect, or how resistive it is to deflection, is the magnetic rigidity, χ. The magnetic rigidity is a

function of the magnitude of the magnetic field, B, and the gyro-radius, ρ, of the particle in the field. It can also be written as a function of the momentum, p, and the charge, q, of the particle, as follows:

$$B\rho = \frac{p}{q}. \tag{2.3}$$

In this experiment, the isotopes being investigated have been stripped of electrons, therefore q can be written as Z, the number of protons in the isotope.

The relativistic momentum of a particle can be written as

$$p = \gamma m_0 \beta, \tag{2.4}$$

where γ is known as the Lorentz factor and m_0 is the mass of the particle being investigated. The Lorentz factor is a function of β, and can be written as

$$\gamma = \frac{1}{\sqrt{1-\beta^2}}. \tag{2.5}$$

Magnetic rigidity can now be written as

$$B\rho = \frac{\gamma m_0 \beta c}{Z}, \tag{2.6}$$

which can be rearranged for m_0,

$$m_0 = \frac{B\rho Z}{\gamma \beta c}. \tag{2.7}$$

Looking at the equation for m_0, it is clear that the only necessary variables needed to find the mass of a particle would be the magnetic rigidity, the time of flight and

the charge of the particle. In this experiment the magnetic field, B, is set for the transporting of a chosen nucleus as the central fragment and is known from the Hall probes used to measure it. The gyroradius has been previously measured. This leaves only the time of flight and Z to be determined to find m_0, meaning the theoretical uncertainty associated with this mass is a function only of time of flight and magnetic rigidity. The uncertainty can be written as follows:

$$\left(\frac{\sigma m}{m}\right)^2 = \left(\frac{\sigma B\rho}{B\rho}\right)^2 + \left(\frac{\sigma TOF}{TOF}\right)^2 \left(1 + \frac{\beta^4}{1-\beta^2}\right). \tag{2.8}$$

2.2 Experimental Facility

This experiment was performed using the projectile FRagment Separator (FRS) facility at GSI in Darmstadt, Germany. GSI, established in 1969, is a unique accelerator facility for heavy ions whose main focus is the investigation into the field of nuclear and atomic physics. It also has applications in materials research, plasma physics, nuclear medicine, and more [13].

GSI employs the use of a linear accelerator (UNILAC) to accelerate ions up to 20% the speed of light using oscillating electric potentials, then sends the ions to a ring synchrotron (SIS18) to further accelerate the ions up to 90% the speed of light. The second acceleration is accomplished through the use of magnetic and electric fields in a circular orbit. These accelerated ions can then be sent to an experimental storage ring (ESR) or into the FRS [13].

The FRS is a magnetic spectrometer with different stages, i.e. four foci (F1, F2, F3, F4). This can be seen is figure 2.1. For this experiment the FRS was operated in the dispersion matching mode where the dispersion of the first section (TA to F2) is

matched by the second section (F2 to F4). The foci F1, F2, F3 are dispersive while F4 is achromatic. By spatially separating the reaction products from the primary beams, isotope selection from the projectile fragments is possible. [4]

Figure 2.1: Schematic setup of the experiment for measuring the mass of ^{33}Mg. [4]

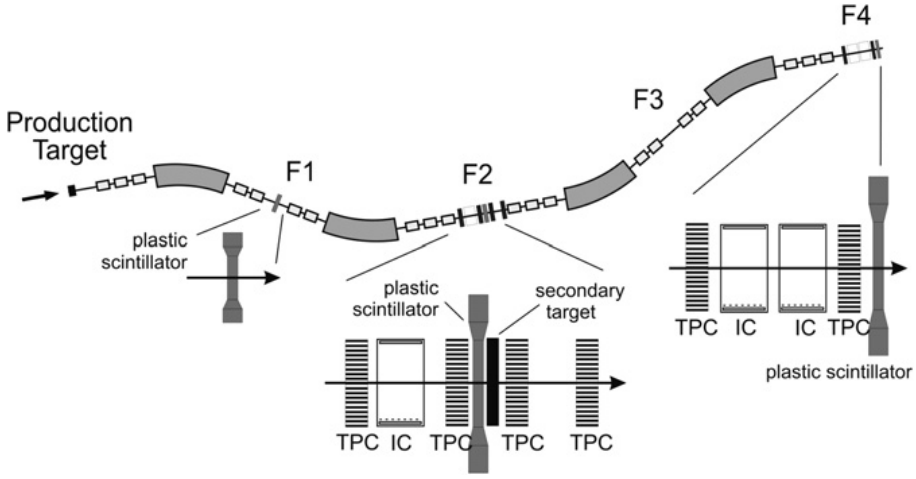

The FRS stages consist of a dipole magnet and sets of quadrupole magnets located in front of and behind the dipoles. The dipole magnets serve to bend the flight path of the projectile fragments according to charge while the quadrupole magnets provide focusing in the x- and y-planes. For the setup of our experiment, a reaction target ladder that allows carbon, CH_2, and empty targets to be inserted into the beam line was used. [4]

2.3 Experimental Set-up

2.3.1 Beam and Target

^{33}Mg, the isotope being investigated in this experiment, is an unstable, short-lived isotope with a half-life of 90.5 ms. As such, it is not found naturally on earth and needs

to be produced in the laboratory for studying its properties. This is accomplished through collisions of stable nuclei. At GSI, a primary beam of ^{48}Ca is accelerated using both the UNILAC and the SIS until the needed energy is reached. The beam is then redirected into the FRS, where it hits a target composed of stable ^{9}Be.

There are a number of reactions products that are produced from this collision. It is therefore necessary to be able to distinguish between one isotope and another before the isotopes reach the secondary reaction target. The first half of the FRS is used for the separation and identification of the incoming nuclei. The identification is done using three kinds of detectors placed in the FRS. The first kind are organic plastic scintillators that are used to measure the time of flight of the particle. Time projection chambers, the second type of detector, are used in conjunction with the scintillators to measure position in the x- and y-directions. Multiple sampling ionization chambers are the last kind of detector in the FRS, and are used to measure the energy loss of the particles passing through.

2.3.2 Plastic Scintillators

Plastic scintillators placed at the F1, F2 (dispersive foci), and F4 stages of the FRS were used to measure the time of flight before and after the reaction target ladder placed at F2. The measured values of the TOF were used to identify the reaction particles and the produced particles.

The scintillators are also used to give a reference timing signal for measuring the drift and delay times of the electrons created through ionization in the TPC. The beam initially passes through the scintillator, inducing a start signal for the timer. The beam then enters the TPC, creating electrons which drift towards drift and delay lines. As the electrons reach those lines, a stop signal is induced. The total

time measured is then equal to the drift/delay time offset by the time it took for the beam to travel from the scintillator to the TPC.

2.3.3 Time Projection Chamber

The Time Projection Chamber (TPC) is used to determine the particle position in the x- and y-directions with a resolution of better than 0.5mm. A single TPC is comprised of an Ar and CH_4 gas filled chamber with an applied electric field, Mylar strips in the drift space, and a copper delay line located at the anodes.

Charged particles enter the chamber, and electrons are created through the ionization of the chamber gas. These electrons drift in an electric field towards the anodes. This drift time through the field allows y-direction particle position determination. As the electrons reach the anode, an induced pulse is sent along the delay line to the left and the right, and using the two signals, the x-position may be determined.

Four TPCs are placed at F2 (dispersive mid-plane) for beam tracking and positioning. Two are placed before the target, and two afterwards in order to track position and angle of the particles both before and after the target reaction. Two TPCs are placed at F4 (achromatic focus) in order to determine position and angle of the incoming particles at the final stage.

2.3.4 Multiple Sampling Ionization Chamber

The MUltiple Sampling Ionization Chambers (MUSIC) are used to determine the the charge of heavy ions. It is comprised of a segmented anode ionization chamber filled with CF_4 gas at room temperature and atmospheric pressure. The MUSIC measures the ionization of the gas in the chamber. This is related to the energy

deposition of the ionizing particles, which is in turn proportional to the square of the charge of the particles.

When an ionizing particle enters the chamber, a cloud of ions and free electrons is generated. An electric field is applied to drift the electrons towards a charge collecting anode. These electrons enter a preamplifier that converts the number of electrons into a signal amplitude that goes through a series of electronics to be analyzed in a computer.

The number of electrons released is proportional to the energy loss of the ionizing particle. The specific energy loss can be written as

$$-\frac{dE}{ds} = \frac{4\pi Z_p^2}{m_e v^2}\left(\frac{e^2}{4\pi\epsilon_o}\right)^2 Z_t N_t \left[\frac{ln(2m_e v^2)}{I} - ln(1-\beta^2) - \beta^2\right] \tag{2.9}$$

where s is the path length through the absorber travelled by the ionizing particle, Z_p and v are the proton number and velocity of the same particle, I is the mean excitation energy of the detector gas. Z_t and N_t are the proton number and particle density of the penetrated material, which in this case, is the detector gas.

Examining equation 2.8, it is clear that the energy loss is proportional to the square of the charge of the isotope. This will allow for particle identification according to Z number. A small correction was made to account for energetic electrons that can cause further ionization in the chamber gas, which causes a slight disparity in the energy lost by the particle and the energy deposition measured by the detector.

The MUSICs are located at F2 and F4 to allow particle identification and counting event by event both before the reaction target and at the final focusing stage. This has useful application advantages in experiments measuring reaction cross sections.

This experiment was originally designed and performed to measure matter radii

through interaction cross-sections and the momentum distribution of ^{33}Mg. The aim of this thesis project is to explore whether it is possible under such measuring conditions to extract the mass of the nucleus using TOF and whether any improvements are technically possible in the experimental setup that may allow future more precise mass measurements.

Chapter 3

Analysis

3.1 Particle Identification

As particles pass through the MUSIC, they deposit energy proportional to their charge, or the number of protons, Z. This energy deposit is in the form of arbitrary units when it reaches the computer, therefore a calibration needs to be done to associate the energy loss with a particular particle.

The energy loss was measured using known isotopes with $A/Z = 2$. By plotting the known value of Z vs the energy loss, a calibration equation can be found that describes the relationship between the two variables. A similar method was used to calibrate the time of flight, resulting in an equation for A/Z that can be used for all particles.

Once this equation has been found, a rough estimate for the value of the energy loss at $Z = 12$ can be found from inspection.

If the energy loss is plotted in the form of a histogram, it presents as a series of peaks, each one corresponding to a different Z. The peak for the Magnesium

isotopes can be found using the value of the energy loss corresponding to $Z = 12$. This selection is shown in Figure 3.1.

Figure 3.1: Energy loss histogram with Magnesium isotopes selected.

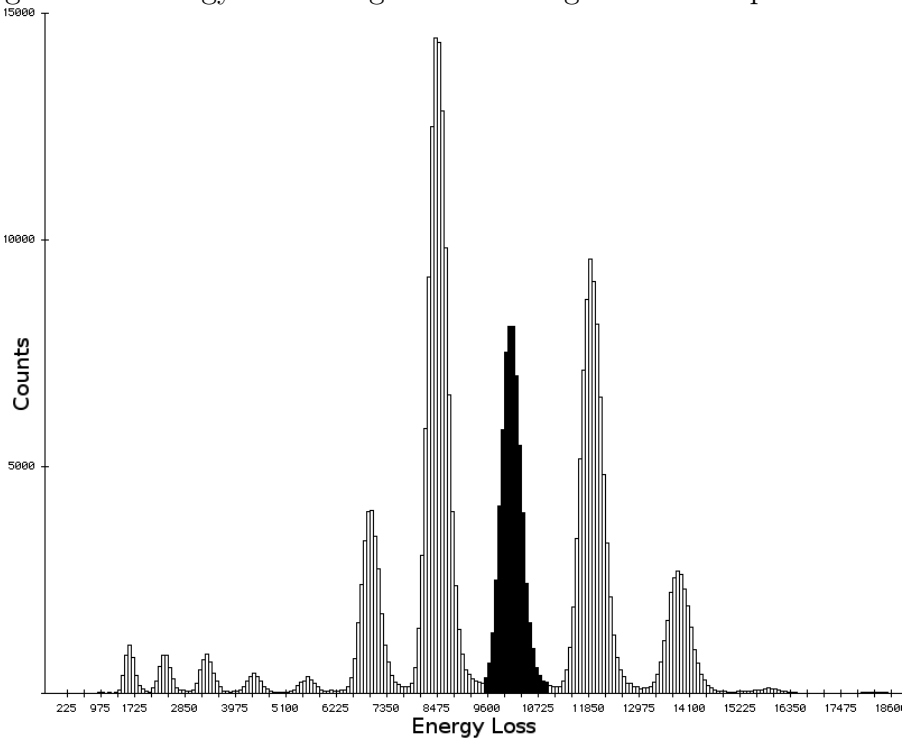

Next, a plot of A/Z, where A is the nucleon number, versus Z can be made in order to distinguish between the magnesium isotopes. Figure 3.2 shows two magnesium isotopes. A/Z for ^{32}Mg = 2.66 and A/Z for ^{33}Mg = 2.75; from this plot, we have identified the magnesium isotopes and we can select ^{3}3Mg.

A slight refinement of the ^{33}Mg selection needs to be performed now to ensure the selection is as pure as possible. F2 is dispersive focus where the position is proportional to the momentum of the incoming particles, allowing the distinction between the magnesium isotopes by plotting the time-of-flight versus the x-position before the target. This can be seen in Figure 3.3.

A second refinement can be accomplished by plotting TOF versus the x-position

Figure 3.2: Close-up of magnesium isotopes in A/Z vs Z plot.

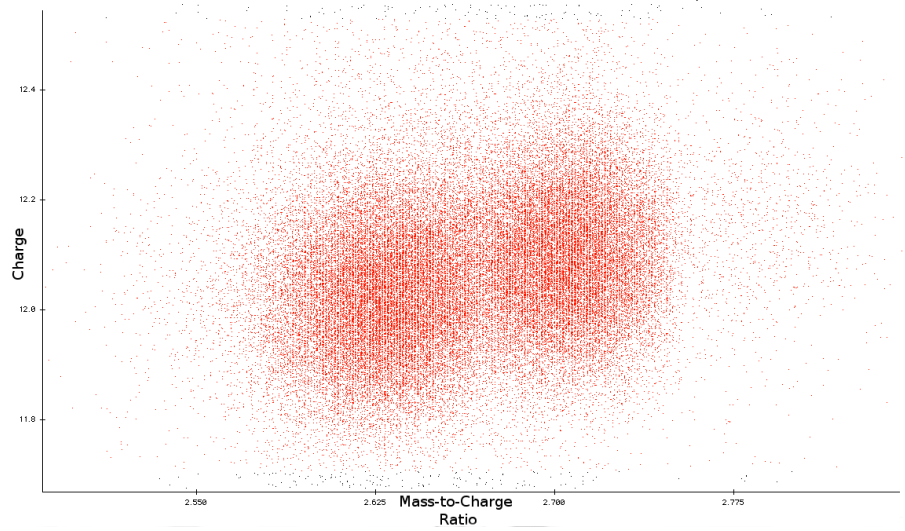

Figure 3.3: Time of flight versus x-position on the target.

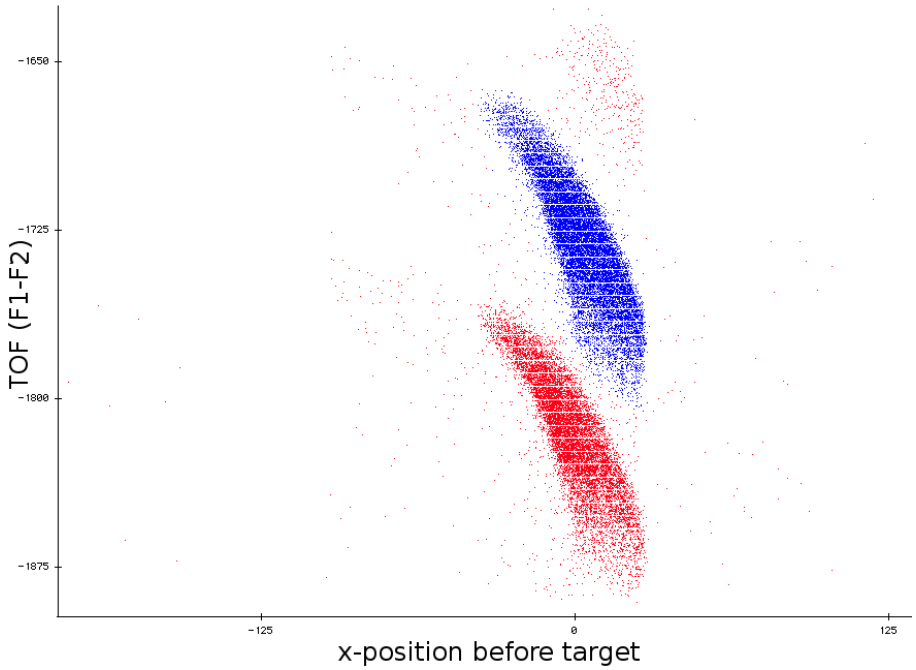

and angle at the focusing plane. This is shown in Figure 3.4.

Figure 3.4: Time of flight versus x-position and angle at the target.

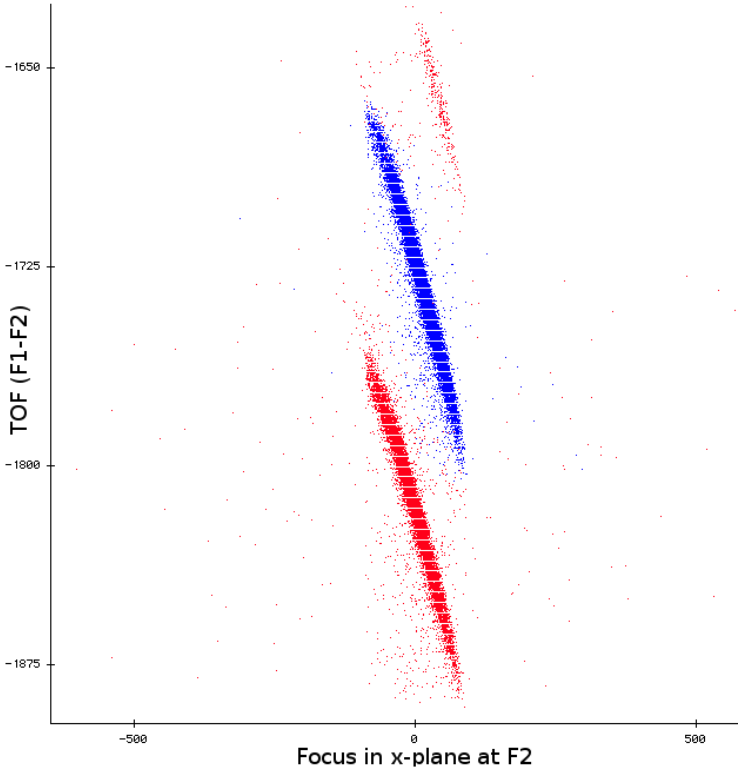

While looking at the TOF between F1 and F2, a third selection refinement step was necessary in some of the runs. This is because there was a tail on the left-hand side of the ^{33}Mg mass peak that was due to a spread in the particles. The position of the particles in the y-direction before the target was examined as well as the angle in the x-direction. In Figure 3.5, TOF versus particle position in the y-direction, a group of particles to the left of the main group of ^{33}Mg can be seen. The selection was refined to exclude those particles. In Figure 3.6, there is a spreading of the particles in the downwards direction. The particles on the lower end of the spread are not due to ^{33}Mg, and may be present due to a spread in momentum causing a contamination in the spread, therefore they were excluded. The selection before and after the third

refinement can be seen in Figure 3.7.

Figure 3.5: TOF of current selection of ^{33}Mg plotted against the position in the y-direction.

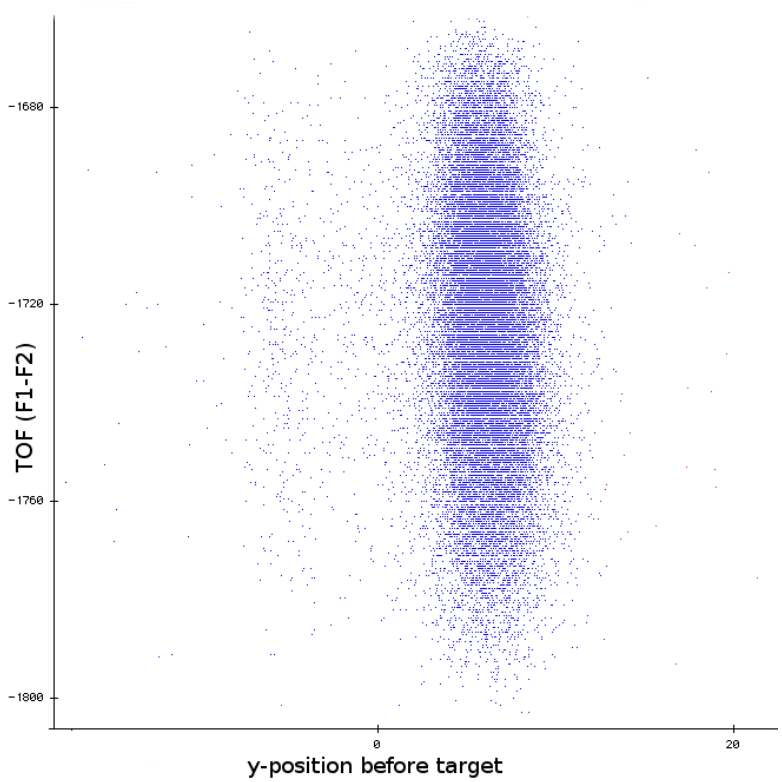

A third refinement for the mass selection from F2 to F4 is necessary for some files as well. When looking at a histogram of the time-of-flight with ^{33}Mg selected, a tail on the right-hand side points to more particles being selected that shouldn't be. The tail corresponds to a spread up and to the left of particles as can be seen in the plot of TOF versus the focusing in the x-plane (Figure 3.8).

3.2 Determining the mass of ^{33}Mg

Using equation 2.7 and the appropriate variables according to the focus points the mass is measured over, the mass can be found. By sorting the mass into a histogram

Figure 3.6: TOF of current selection of ^{33}Mg plotted against the angle in the x-direction before the target.

Figure 3.7: Mass refinement before and after the third refinement for particles being measured between F1 and F2.

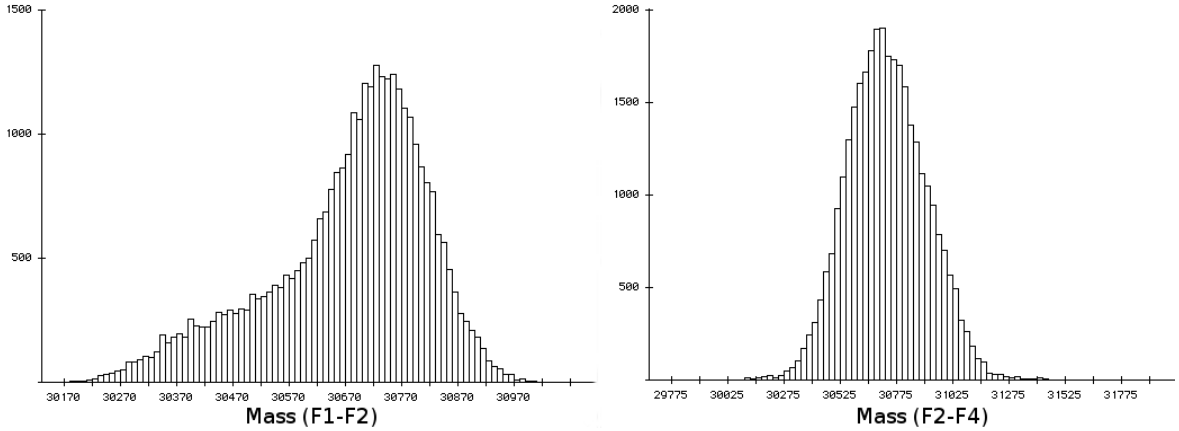

Figure 3.8: TOF from F2 to F4 plotted versus the focusing in the x-direction. There is a spread in particles upwards and to the left.

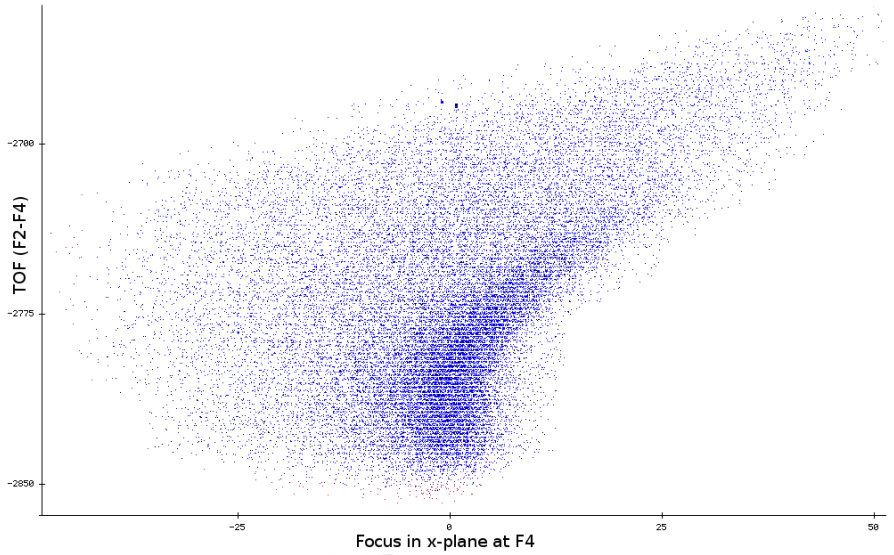

and then applying the refined selection from the previous section, a distribution of the value of the mass of ^{33}Mg can be found, as seen in Figure 3.9.

The mass was found by fitting a Gaussian curve to the mass peak. This was done using the TOF from F1 to F2 and F2 to F4. Table 3.2 contains the Gaussian fit results for TOF measured from F1 to F2. Table 3.2 contains the fit results for TOF measured from F2 to F4. In these tables, σ is one standard deviation of the distribution, and N is the total integrated counts in the peaks.

Run	Peak Amplitude	N	Mass (MeV/c^2)	σ
218-220	1084.77	28386	30736.6	102.934
235-236	652.765	18502	30711.4	115.390
244-245	450.585	12608	30711.8	114.913
341-345	950.790	17178	30749.7	72.3767
347-351	1160.43	21723	30743.0	74.7682
352-356	987.213	18634	30749.7	75.7876
357-360	687.088	12822	30743.0	74.6318

Table 3.1: Gaussian fit results for mass of ^{33}Mg measured using TOF from F1 to F2.

Figure 3.9: Mass histogram with ^{33}Mg selection.

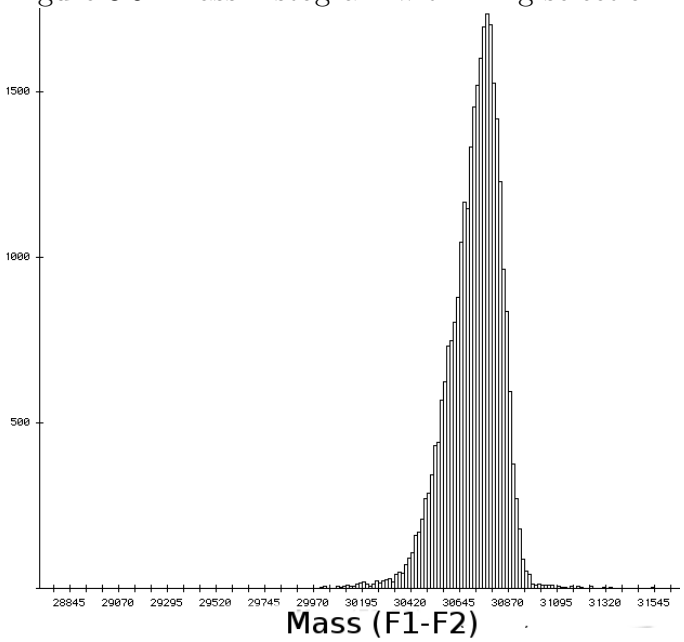

The data from each run was added together, and another Gaussian fit was performed in order to find the mass. Final values for the mass were found to be:

$$m_{F1-F2} = 30740.8 \pm 0.2\, MeV/c^2$$

$$m_{F2-F4} = 30707.9 \pm 0.5\, MeV/c^2$$

The uncertainties in the above equations are the statistical uncertainties associated with the peaks. The equation

$$\sigma_m = \frac{\sigma}{\sqrt{N_{tot}}},$$

where N_{tot} is the total integrated counts in the peak, was used to calculate the uncertainties. The resolutions of the above mass values are 0.28% (F1 to F2) and 0.58% (F2 to F4) in terms of σ. The accepted value for the mass of ^{33}Mg is 30744.2 $\pm$

Run	Peak Amplitude	N	Mass (MeV/c^2)	σ (MeV/c^2)
218-220	1805.93	26161	30678.6	176.211
235-236	1351.00	19933	30683.1	179.406
244-245	936.131	13585	30692.7	177.091
341-345	1356.0	32280	30730.4	169.667
347-351	1363.52	34072	30713.0	173.122
352-356	1398.37	32866	30732.3	165.04
357-360	824.88	18245	30734.4	165.171

Table 3.2: Gaussian fit results for mass of ^{33}Mg measured using TOF from F2 to F4.

0.0195614 MeV/c^2. In order to look at how much each of the components of the mass are contributing to the experimental uncertainty, it is of interest to look at the uncertainties and resolutions associated with each.

The value for the resolution of TOF was found by taking a small slice out of the ^{33}Mg selection of TOF, and doing a Gaussian fit across all runs to find the resolution. The resolution for the TOF between F1 and F2 was found to be 1.03% (in terms of sigma) and between F2 and F4 it was found to be 0.75%.

From here, the uncertainty in the time of flight can be found by rearranging the following equation:

$$R = \frac{\sigma_{TOF}}{TOF} * 100,$$

where R is the resolution, σ_{TOF} is the uncertainty in the time-of-flight and TOF is 68 ns for F1 to F2 and 145 ns for F2 to F4.

From the above equation, it is found that

$$\sigma_{TOF12} = 0.7004\, ns,$$

$$\sigma_{TOF24} = 1.0875\, ns.$$

These uncertainties are larger than expected and could have arisen in part due to magnetic rigidity setting, which would cause a spread in the momentum of the particles at the focus.

If a TOF resolution of 50 ps could be achieved, a theoretical uncertainty for the mass value of 0.220 MeV/c^2 for F1 to F2 and 0.094 MeV/c^2 for F2 to F4 could be had, assuming the magnetic rigidity is accurate.

There is a possibility that the mass peak has been shifted, by 3.4 MeV/c^2 in F1 to F2 and by 36.3 MeV/c^2 in F2 to F4. Using a TOF resolution of 50 ps, and the associated mass uncertainties from above, a TOF shift of 0.11 ns would be necessary for F1 to F2 and a shift of 0.04 ns would be needed for F2 to F4 to get the accepted value for the mass of ^{33}Mg. This calculation was done assuming the magnetic rigidity was accurate.

The one-neutron separation energy was found using the equation

$$S_n = ({}^{32}Mg + n - {}^{33}Mg)c^2$$

for the masses.

For F1 to F2, S_n = 5.25 MeV/c^2 and for F2 to F4, S_n = 38.79 MeV/c^2. The accepted value, taken from the NNDC database has $S_n = 2.22$ MeV/c^2. This difference in energy could again be due the uncertainties in calibration or resolution of the TOF and possibly due to the magnetic rigidity setting.

Chapter 4

Discussion

In this experiment, the mass of ^{33}Mg was measured directly using a time-of-flight technique. The results indicate that there are some issues that need to be resolved in order to obtain more accurate and precise results.

A potential source of uncertainty in this experiment is the accuracy of the magnetic rigidity setting. The magnetic rigidity of the the setup was set to assume ^{33}Mg was the central fragment, and any sort of inaccuracy would result in a spread in momentum at the focus. This momentum spread would cause a worsening in the resolution of the time-of-flight, which would propagate through to the mass.

Uncertainty could also have arisen from the absolute calibration for the beta value. Inaccuracies in this value could contribute to the observed shift in the mass peak.

For further understanding of ^{33}Mg, and the uncertainties associated with this experiment, it would be useful to perform this experiment on other various known masses in order to get an estimate of the uncertainty associated with this experiment.

One of the goals of this experiment was to gain an understanding of the N=20 shell closure breakdown. Data taken from the NNDC [10] shows the one neutron

separation energy for ^{33}Mg to be 2210 keV. The data obtained in this experiment did not agree with these values, which indicates a need for improvement in the mass determination and resolution. There is a significant mass difference observed when measuring from F1 to F2 and F2 to F4, suggesting an inconsistent setting in the set-up or problem of some sort that could be isolated to one section.

While this experiment was unable to accurately measure the mass of ^{33}Mg, the resolution was comparable to previous experiments. These results suggest that through further optimization and calibration this method has the potential to be used in future experiments.

Chapter 5

Conclusion

A direct measurement of the mass of ^{33}Mg was performed through a time-of-flight technique using FRS at GSI in order to determine the feasibility of this method. ^{33}Mg was chosen in order to examine the shell closure at N=20. The mass found in this experiment did not agree to within uncertainty with the accepted value. However, through further optimization this method has the potential to be an acceptable technique.

Bibliography

[1] T. Baumann. PhD thesis, University of Giessen, 1999. Ph.D. Thesis.

[2] Richard A. Dunlap. *An introduction to the physics of nuclei and particles*, chapter 4, 5, pages 28–60. David Harris, 2004.

[3] L. Gaudefroy, W. Mittig, N.A. Orr, S. Varet, M. Chartier, et al. *Physical Review Letters*, 109:202–503, 2012.

[4] R. Kanungo, C. Nociforo, A. Prochazka, Y. Utsuno, T. Aumann, D. Boutin, D. Cortina-Gil, B. Davids, M. Diakaki, F. Farinon, H. Geissel, R. Gernhuser, J. Gerl, R. Janik, B. Jonson, B. Kindler, R. Knbel, R. Krcken, M. Lantz, H. Lenske, Y. Litvinov, K. Mahata, P. Maierbeck, A. Musumarra, T. Nilsson, T. Otsuka, C. Perro, C. Scheidenberger, B. Sitar, P. Strmen, B. Sun, I. Szarka, I. Tanihata, H. Weick, and M. Winkler. *Physics Letters B*, 685(4-5):253–257, March 2010.

[5] D. Lunney, G. Audi, C. Gaulard, M. de Saint Simon, C. Thibault, and N. Vieira. *Eur. Phys. J. A 28, 129138*, 2006.

[6] D. Lunney, J.M. Pearson, and C. Thibault. *Rev. Mod. Phys.*, 75(3):1022–1074, July 2003.

[7] W. Mittig, A. Lepine-Szily, and N. A. Orr. *Annu. Rev. Nucl. Sci*, pages 27–66, 1997.

[8] N.A. Orr, W. Mittig, L.K. Fifield, M. Lewitowicz, PIagnol E., Y. Schutz, Zhan Wen Long, L. Bianchi, A. Gillibert, A.V Belozyorov, S.M. Lukyanov, YxxE. Pcnionhkevich, A.C.C. Villari, A. Cunsolo, A. Foti, G. Audi, C. Stephan, and L. Tasson-Got. *Physics Letters B*, 258:29–34, May 1991.

[9] C. Scheidenberger. *European Physical Journal A*, 15:7–11, October 2002.

[10] Unknown. Chart of nuclides. Online. http://www.nndc.bnl.gov/chart/, Accessed March 16th, 2013.

[11] Unknown. Collective model, (2013). http://www.britannica.com, 6 March 2013.

[12] Unknown. Penning traps. 11 March 2013.

[13] Unknown. Research at GSI. https://www.gsi.de/en/researchaccelerators.htm, 21 February 2013.